Supplementary Information

Controllable Patterning of magnetic bits with atomically sharp boundaries

Qi Wang[1,2,3], Lei Jin[4], Dongsheng He[5], Hideto Yanagihara[6,7,8], Eiji Kita[6], Rafal E. Dunin-Borkowski[4], Fu-Rong Chen[1,2,3], Xiaoyan Zhong[1,2,3*]

1 TRACE EM Unit, Department of Materials Science and Engineering and Hong Kong Institute for Clean Energy (HKICE), City University of Hong Kong, Kowloon, Hong Kong SAR, People's Republic of China.

2 City University of Hong Kong Matter Science Research Institute (Futian, Shenzhen), 518048, Shenzhen, People's Republic of China.

3 Nanomanufacturing Laboratory (NML), City University of Hong Kong Shenzhen Research Institute, 518048, Shenzhen, People's Republic of China.

4 Ernst Ruska-Centre for Microscopy and Spectroscopy with Electrons, Forschungszentrum Jülich GmbH, 52425 Jülich, Germany

5 Core Research Facilities, Southern University of Science and Technology, Shenzhen 518055, People's Republic of China.

6 Department of Applied Physics, University of Tsukuba, Tsukuba, Ibaraki, 3058573, Japan

7 Tsukuba Research Center for Energy Materials Science (TREMS), University of Tsukuba, Tsukuba, Ibaraki, 3058573, Japan

8 Tsukuba Research Center for Organic-Inorganic Quantum Spin Science and Technology (OIQSST), University of Tsukuba, Tsukuba, Ibaraki, 3058573, Japan

* corresponding author: Xiaoyan Zhong, xzhong25@cityu.edu.hk

Supplementary Fig. 1 Structural and Crystallographic Characterization.
(a) HAADF-STEM image of a 10-nm-thick $NiFe_2O_4$ thin film epitaxially grown on an $MgAl_2O_4$ substrate — the sample used in this paper. Scale bar, 5 nm. (b) Classification of the cationic sites based on their spatial configuration. A-sites are octahedral sites with double the projected atomic density, B-sites are standard octahedral sites, C-sites are tetrahedral sites, and D-sites are newly formed octahedral sites in the Rock-salt phase. **(c)** Example of a statistical analysis histogram for one frame. (d) Experimental Fast Fourier Transform (FFT) of the pristine Spinel structure. (e) Experimental FFT of the final Rock-salt structure. The yellow circles highlight the systematic absence of specific Spinel reflections. (f) Superposed simulated kinematic diffraction patterns for the Spinel (red) and Rock-salt (blue) structures. Blue circles mark reflections unique to the Spinel phase, consistent with the experimental FFTs. (g) Long-term structural stability assessment. High-resolution HAADF-STEM imaging acquired before and after 24 days of ambient storage confirms the robust preservation of the patterned domains and the atomic sharp interfaces, exhibiting no signs of spontaneous structural recovery. Scale bar, 5 nm.

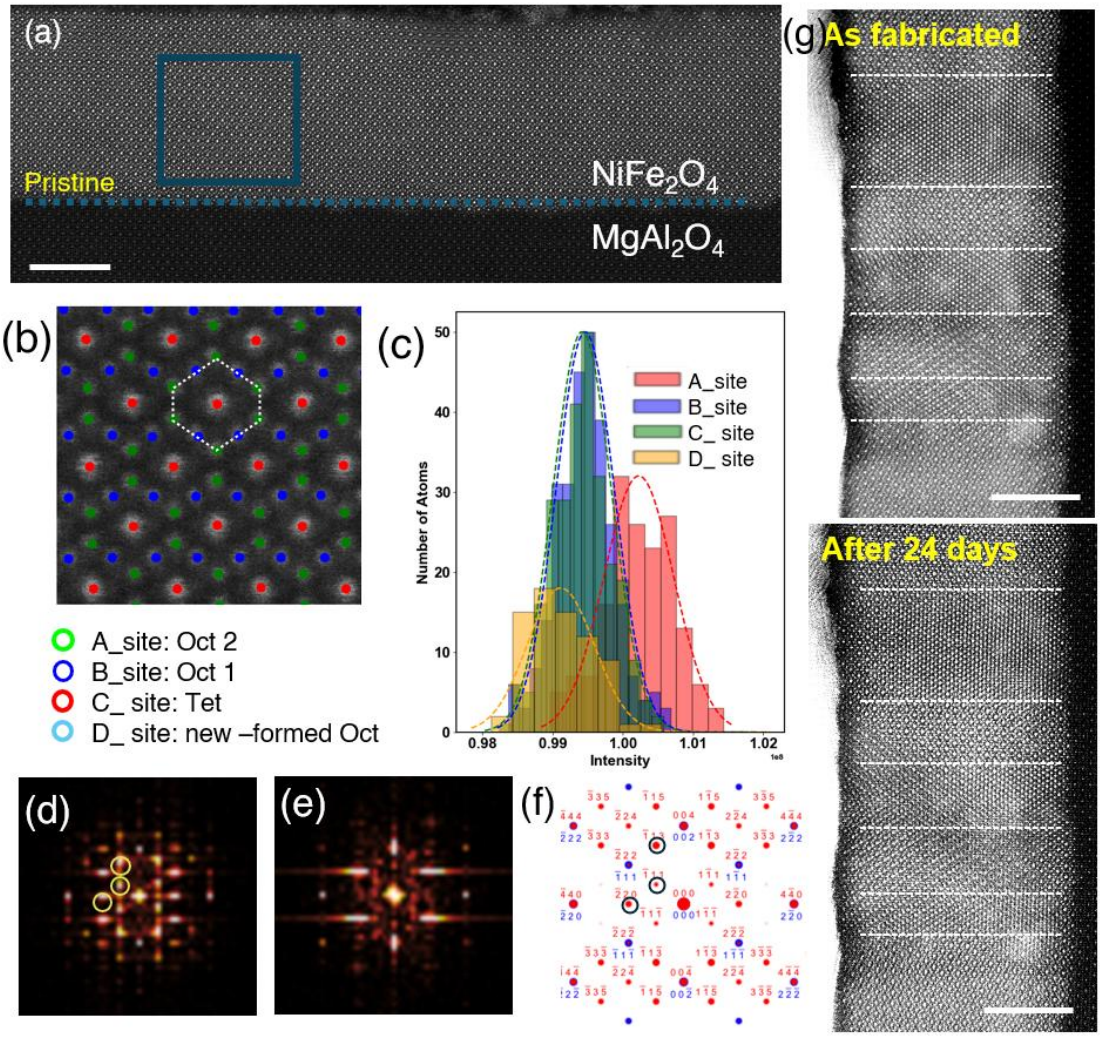

Supplementary Fig. 2 Simulation of Oxygen Vacancy in iDPC and dDPC.
(a) Atomic model of a Spinel $NiFe_2O_4$ supercell containing an engineered oxygen vacancy (indicated by green arrows). **(b)** Simulated iDPC images of the oxygen-deficient structure. The green circle highlights the marked reduction in column intensity at the vacancy site. **(c)** Simulated dDPC of the oxygen-deficient structures, with the white circle also indicating reduced intensity in vacancy position. Scale bar, 0.25 nm.

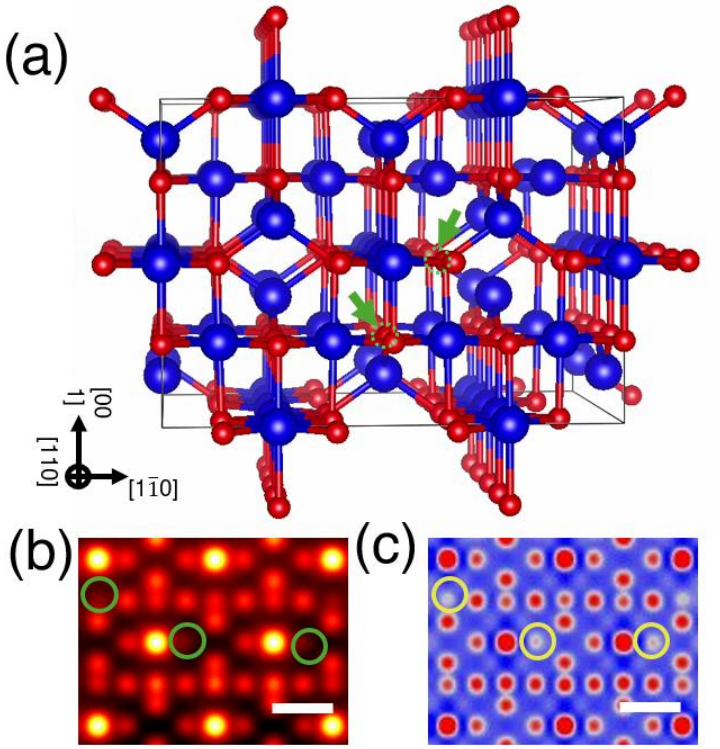

Supplementary Fig. 3 Real-time 4D-STEM analysis of phase transition dynamics. (a) ADF images showing rearrangement of cation atom, (b) electric field vector fields (c) charge density distribution maps, and (d) iDPC-STEM images revealing projected electrostatic potential changes at initial, intermediate, and final stages of the phase transition. (e) Experimental charge density line profile obtained from the black-framed atomic column in (c), showing corresponding reduction in charge density at the oxygen column (black arrow). (f) Experimental iDPC intensity line profile extracted from the blue-framed atomic column in (d), demonstrating intensity reduction at the oxygen column (blue arrow).

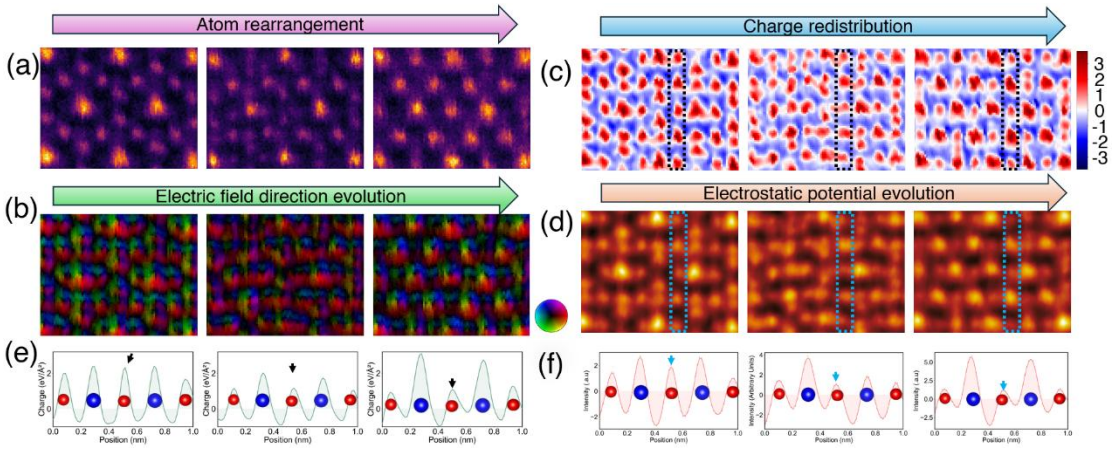

Supplementary Fig. 4 Time-Resolved EDS Elemental Mapping.
Atomic-resolution EDS maps showing the Fe (red) and Ni (blue) cation distributions at the initial, intermediate, and final stages of the phase transition, visualizing the cationic rearrangement pathway. Scale bar, 1 nm.

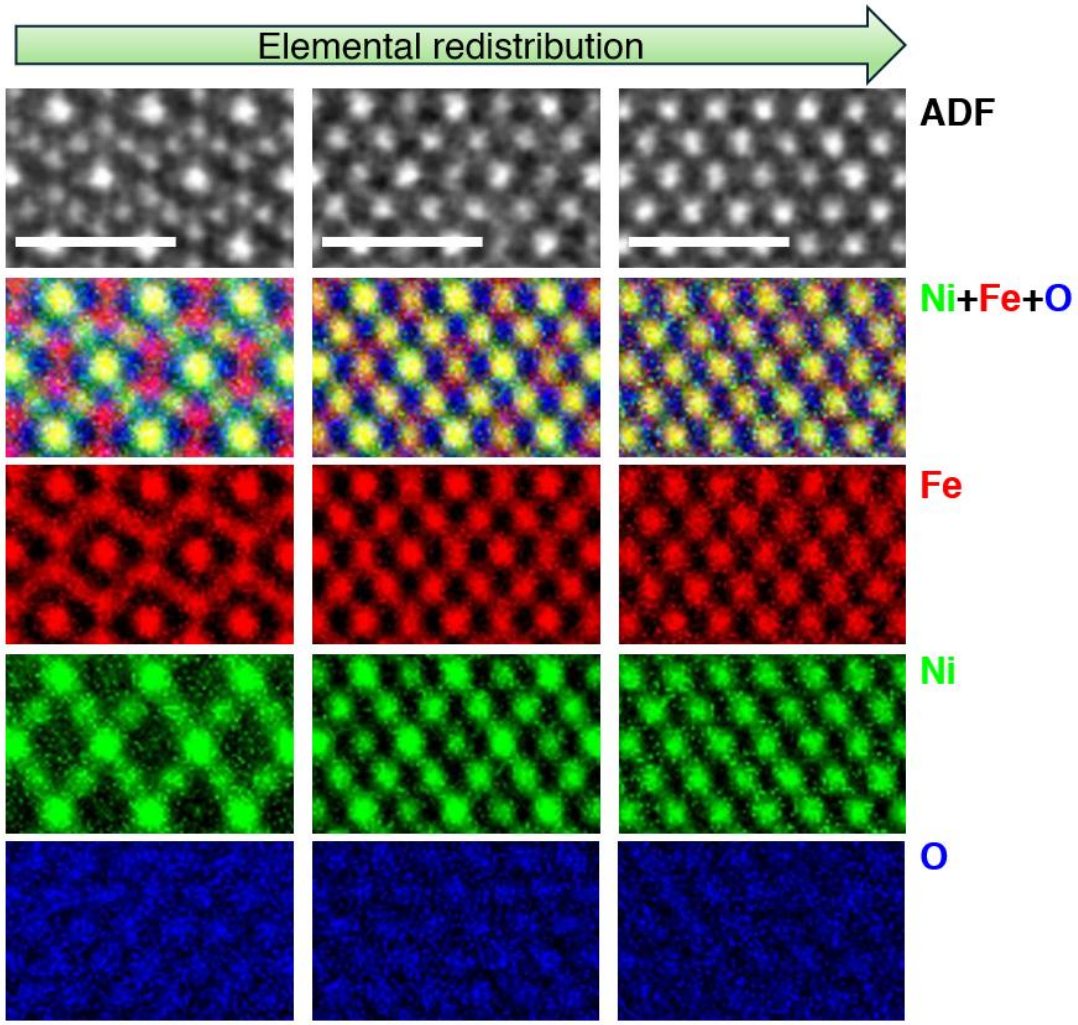

Supplementary Fig. 5 Quantitative EDS Analysis of Oxygen Stoichiometry.
EDS spectra acquired from the (**a**) initial Spinel and (**b**) final Rock-salt phases. The quantitative analysis confirms that the conversion involves a net reduction in the oxygen-to-metal atomic ratio.

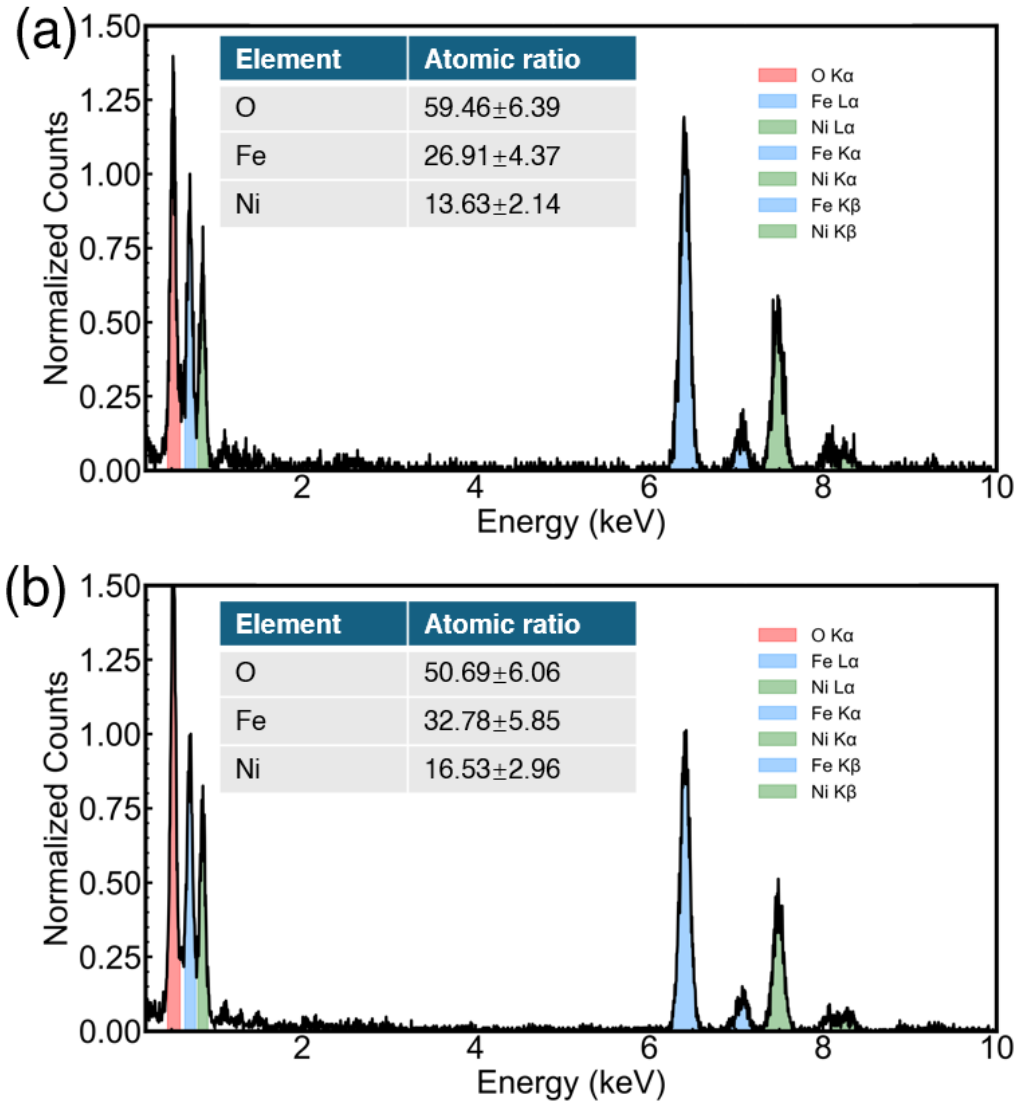

Supplementary Fig. 6 Detailed Time-Resolved EELS Analysis.

EELS spectra of the **(a)** O K-edge, **(b)** Fe L-edge, and **(c)** Ni L-edge, shown for the initial, intermediate, and final stages of the phase transition. **(d)** The evolution of the Fe L_3/L_2 ratio. Its decrease from 4.8 to 3.3 is a definitive signature of Fe valence reduction from +3 towards +2.

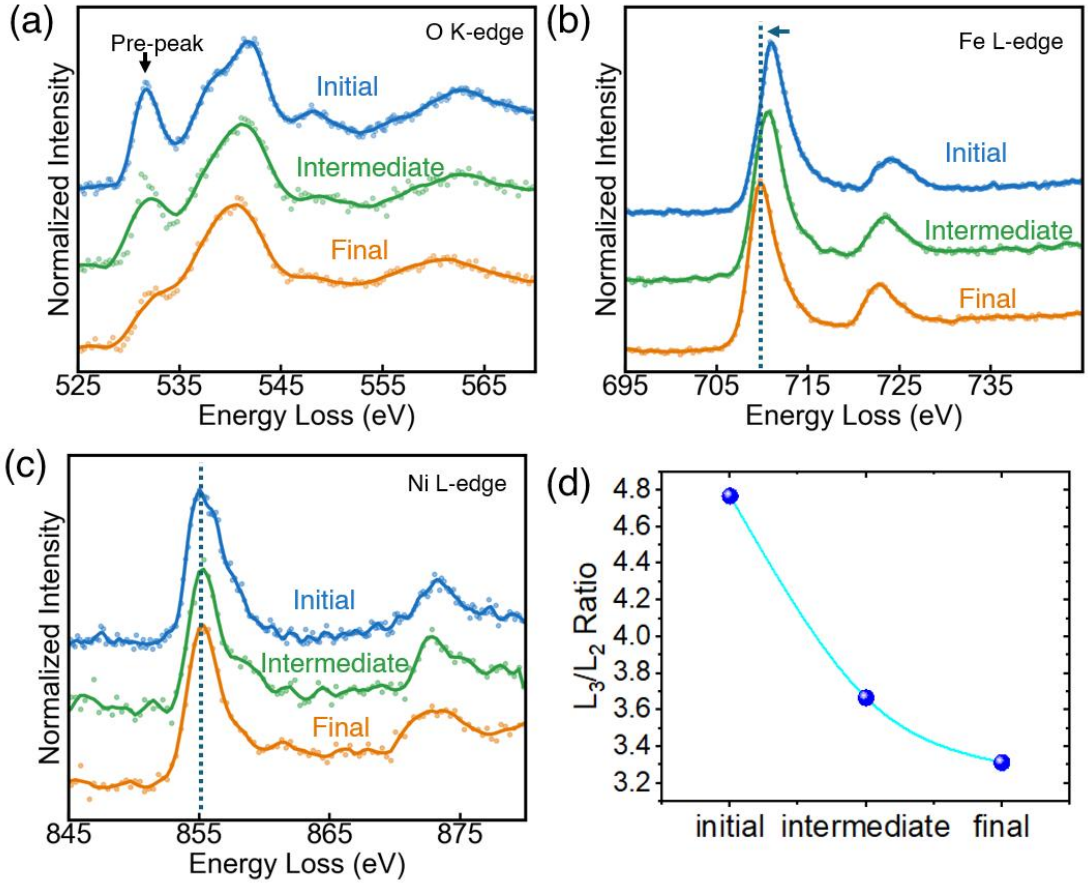

Supplementary Fig. 7 Quantitative Analysis of Phase Transformation Kinetics.
(a) ADF images of the fabrication area at 0s and 268s. Scale bar, 2 nm. **(b-e)** The intensity distribution of **(b)** A-sites, **(c)** B-sites, **(d)** C-sites, and **(e)** D-sites over 270s.

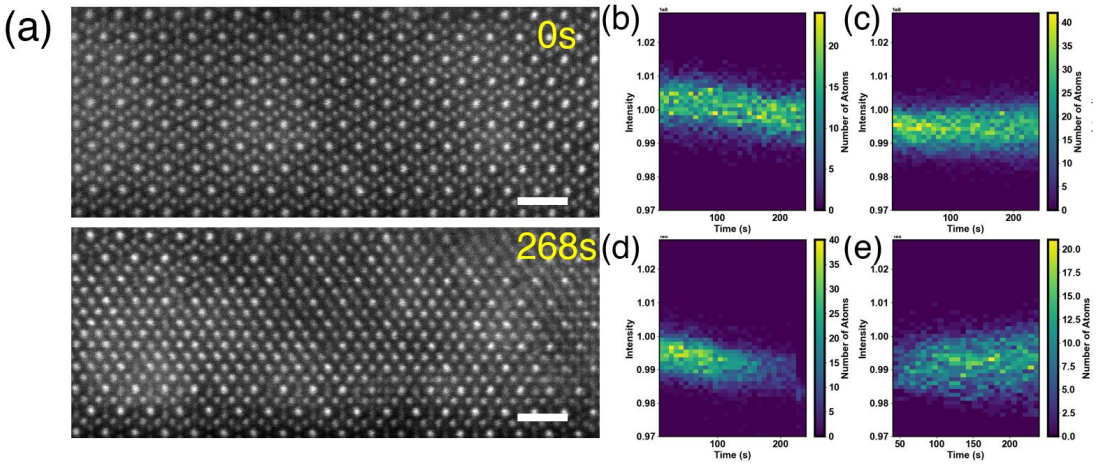

Supplementary Fig. 8 Summary of Statistical Site Intensity Analysis.
A comprehensive summary of the statistical distributions of the A, B, C, and D site intensities for all frames acquired during the real-time monitoring of the phase transition.

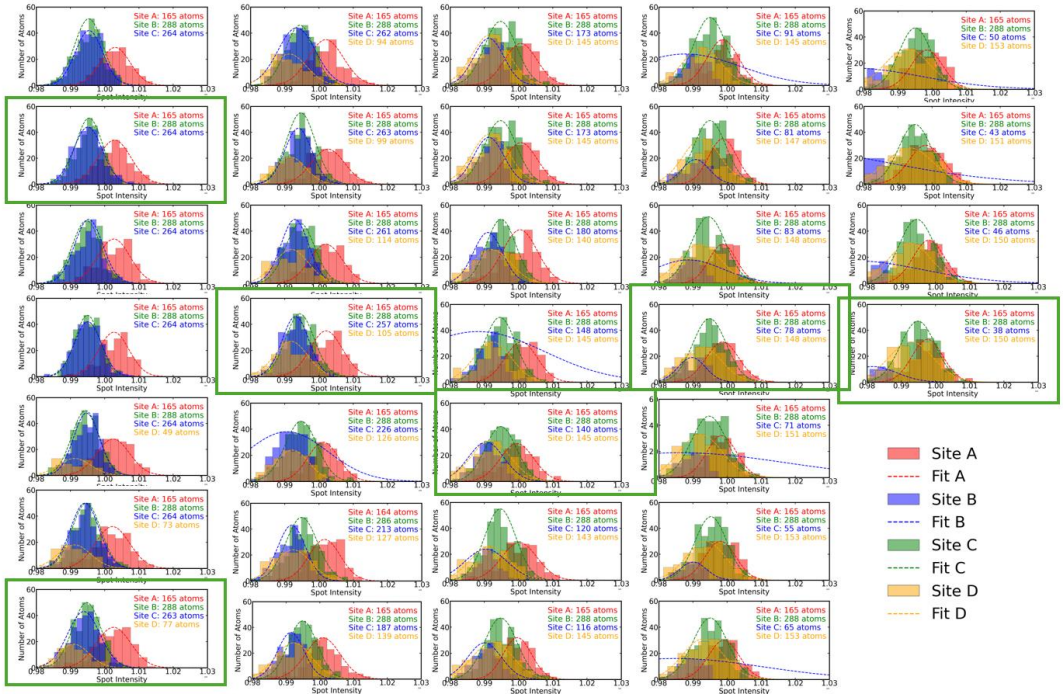

Supplementary Fig. 9 Size-Dependent Raw EMCD Spectra for the Fe L-edge.
(a) A representative STEM image showing an array of fabricated bits of varying sizes. Scale bar: 2nm. **(b-g)** The raw-data positive "+" electron energy-loss (EEL) spectra in red, the negative "-" EEL spectra in blue and the EMCD spectra in green for the Fe L-edge for a series of bits with progressively decreasing size. The corresponding bit structure is shown alongside each spectrum.

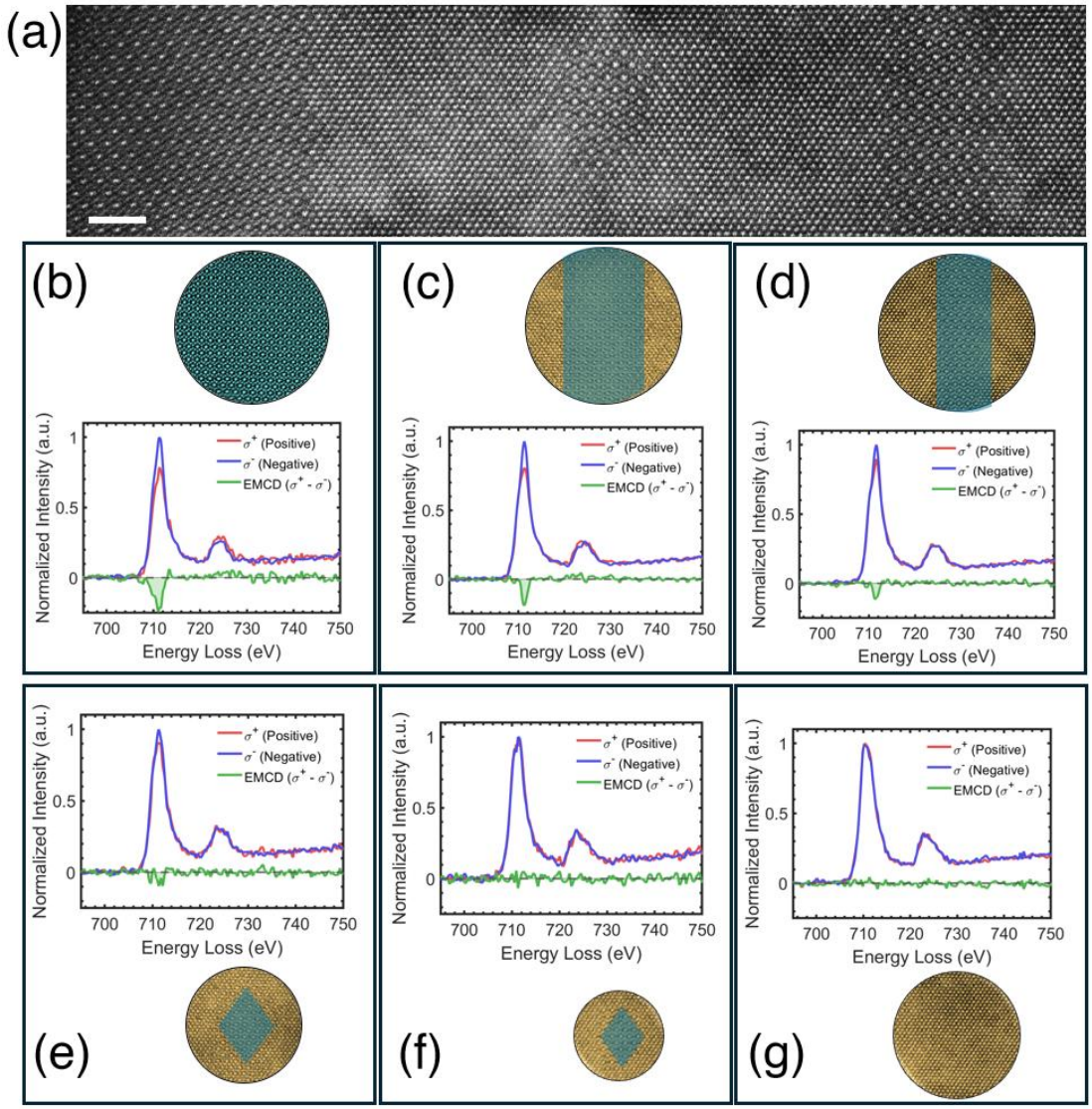

Supplementary Fig. 10 Size-Dependent Raw EMCD Spectra for the Ni L-edge.
(a-f) The raw-data positive "+" electron energy-loss (EEL) spectra in red, the negative "-" EEL spectra in blue and the EMCD spectra in green for the Ni L-edge for a series of bits with progressively decreasing size.

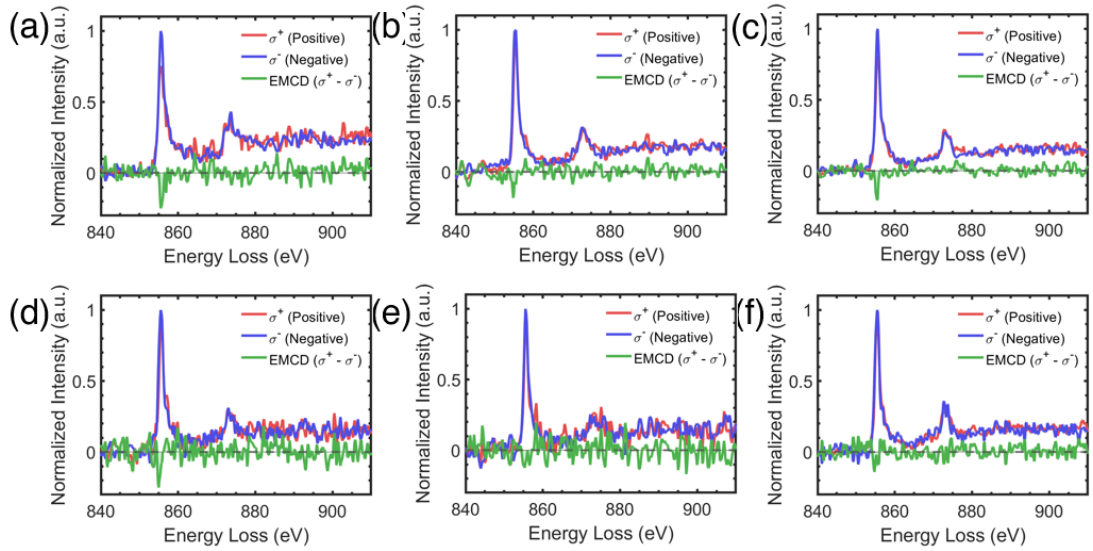

Supplementary Fig. 11 Micromagnetic simulations demonstrating enhanced thermal stability and coercivity via AFM interfacial coupling. (**a**) Schematic representation of the geometric models used for micromagnetic simulations: an isolated purely ferrimagnetic (FM) $NiFe_2O_4$ bit (top) and an FM $NiFe_2O_4$bit completely embedded within an antiferromagnetic (AFM) matrix (bottom). (**b-c)** Simulated magnetic hysteresis loops for varying lateral sizes (ranging from 3 nm to 11 nm) of (**b**) the isolated FM bits and (**c**) the AFM-embedded bits. The horizontal arrows explicitly highlight the significant broadening of the hysteresis loop at the 3 nm scale for the embedded structure (red arrow) compared to the isolated structure (blue arrow), indicating enhanced resistance to magnetization reversal. (**d)** Extracted coercivity (H_c) as a function of the bit size. The red curve (with AFM matrix) consistently exhibits substantially higher coercivity than the blue curve (without AFM matrix) across all dimensions, quantifying the additional pinning anisotropy provided by the interfacial exchange coupling. (**e, f)** Three-dimensional spatial mapping of the magnetic spin vectors for an 11 nm lateral size bit. (**e**) The bit embedded in the AFM matrix maintains a strictly ordered, stable single-domain state. (**f**) In contrast, the purely isolated bit exhibits a randomized, chaotic magnetic vector distribution, signifying the loss of long-range magnetic order due to thermal fluctuations without interfacial protection.